The calibration and validation of a model for simulating the thermal and electrical performance of a 1 kW$_{AC}$ proton-exchange membrane fuel-cell micro-cogeneration device

Geoffrey Johnson [a,*], Ian Beausoleil-Morrison [a], Bruce Strathearn [b], Erik Thorsteinson [b], Tom Mackintosh [b]

[a] *Sustainable Building Energy Systems, Faculty of Engineering and Design, Carleton University, Ottawa, Canada K1S 5B6*
[b] *Renewable and Integrated Energy Systems, CanmetENERGY, Natural Resources, Ottawa, Canada*

HIGHLIGHTS

▶ We adapted an existing micro-cogeneration model to represent a PEMFC.
▶ We conducted tests to characterize the performance of a PEMFC.
▶ We calibrated and validated the model of the PEMFC with experimental data.

ARTICLE INFO

ABSTRACT

The cogeneration of heat and electricity using small-scale fuel-cell devices may lead to reduced energy consumption, lower greenhouse gas emissions, and less reliance on the central electrical grid. Without accurate methods to simulate thermal and electrical production concurrently with the operation of coupled plant components and the demands of the host building and its occupants, these potential benefits can not be fully assessed nor can the deployment of fuel-cell micro-cogeneration be optimally configured. Enhancements are proposed to an existing fuel-cell micro-cogeneration model and then its calibration is demonstrated using empirical data gathered from experiments conducted with a 1.0 kW$_{AC}$ PEMFC micro-cogeneration device. The experimental configuration, types of instrumentation employed, and the operating scenarios examined are treated. The calibration coefficients necessary to accurately simulate the thermal and electrical performance of this device are presented and then the validity of the model's functional form and its calibration are assessed through the comparison of model predictions to measurements from a disjunct set of 10 tests.

1. Introduction

The production of combined heat and electric power on a residential scale (<15 kW$_{AC}$) from a single fuel source is known as micro-cogeneration. Micro-cogeneration systems have the potential to reduce energy demands of the residential sector for space heating, domestic hot water heating, and electricity. Reduced greenhouse gas emissions and reduced reliance upon central electrical generation, transmission, and distribution systems are possible benefits. An overview of the micro-cogeneration field is provided in Refs. [1] and [2].

Fuel cells can form the basis of a micro-cogeneration system. In order to be viable, fuel-cell based micro-cogeneration systems must be competitive with current combined-cycle fossil fuel power plants that have net electrical efficiencies of approximately 55% relative to the fuel's lower heating value (LHV) [3,4]. As fuel-cell micro-cogeneration is unlikely to achieve this electrical efficiency level, the effective use of the heat production is necessary to compete with efficient central power plants.

Building performance simulation (BPS) can be used to assess the benefits of fuel-cell based micro-cogeneration systems. By using BPS methods it is possible to simulate complex interactions involving micro-cogeneration systems, occupant behavior, building envelopes, climate data, control systems and conventional

* Corresponding author.
  E-mail addresses: gjohnso2@connect.carleton.ca (G. Johnson), Ian_Beausoleil-Morrison@carleton.ca (I. Beausoleil-Morrison), Bruce.Strathearn@nrcan-rncan.gc.ca (B. Strathearn), Erik.Thorsteinson@nrcan-rncan.gc.ca (E. Thorsteinson), Tom.Mackintosh@nrcan-rncan.gc.ca (T. Mackintosh).

residential heating, ventilating, and air conditioning equipment. Annex 42 of the International Energy Agency's Energy Conservation in Buildings and Community Systems Programme (IEA/ECBCS) [5] was founded to develop the tools that are necessary to use BPS to assess the benefits of micro-cogeneration systems.

Efforts by Annex 42 members led to the development of a fuel-cell micro-cogeneration model for implementation into BPS tools. In this model the system is discretized into control volumes whose boundaries exchange energy and mass flows. A schematic representation of the Annex 42 model illustrating the control volumes and their interactions is provided in Fig. 1.

Although first conceived for modeling solid-oxide fuel-cell (SOFC) micro-cogeneration devices [6], the model was later expanded [7] to consider proton-exchange membrane fuel-cell (PEMFC) devices as well. By exercising the appropriate combination of control volumes the model can be configured to represent either SOFC or PEMFC micro-cogeneration devices. The model represents the following sub-systems:

- A fuel-cell power module (FCPM) that produces heat and DC power. The control volume representing the FCPM includes the anode/cathode stack as well as fuel reforming components (see Ref. [7] for details).
- A power conditioning unit (PCU) that converts DC power produced by the FCPM to AC power.
- The internal components that consume AC power (AC ancillaries) other than the PCU.
- A fuel-cell housing that loses heat to the surrounding environment.
- An air supply system that provides the necessary oxygen to support the reforming and electrochemical reactions that take place in the FCPM.

- A system that supplies fuel to support the reactions that take place in the FCPM.
- A gas-water heat exchanger to recover thermal energy from the FCPM's product gases in SOFC devices.
- A water–water heat exchanger to recover thermal energy from PEMFC devices.

The Annex 42 model represents the behavior of the individual sub-systems using empirical data gathered from experiments conducted with coherent fuel-cell micro-cogeneration devices rather than employing theoretical thermodynamic and chemical relations. A demonstration of this calibration procedure is provided in Ref. [8], which shows how data from a series of 45 steady-state and transient tests were utilized to calibrate the Annex 42 model to represent the behavior of a 2.8 kW$_{AC}$ SOFC micro-cogeneration device. The calibration of the Annex 42 model performed in Ref. [8] was validated in Ref. [9] using data from 16 additional experiments that were disjunct from those employed in the calibration. An alternate calibration approach was taken by Ref. [10], who employed a detailed SOFC chemical process model to calibrate the Annex 42 model for hypothetical micro-cogeneration devices.

Recently, numerous researchers have contributed to the modeling of PEMFC micro-cogeneration devices. In Ref. [11] a model is developed and used to simulate PEMFC performance on an annual basis in rural Venezuela. However, this model may not be sufficiently detailed for BPS simulation on smaller time scales. References [12–16] describe models that focus on simulating the electrochemical processes within the PEMFC. The goal of these models has been to provide guidance to PEMFC designers and they are not intended for direct use with BPS, although it might be possible to use their results to eventually calibrate the Annex 42 model (as was done in Ref. [10]).
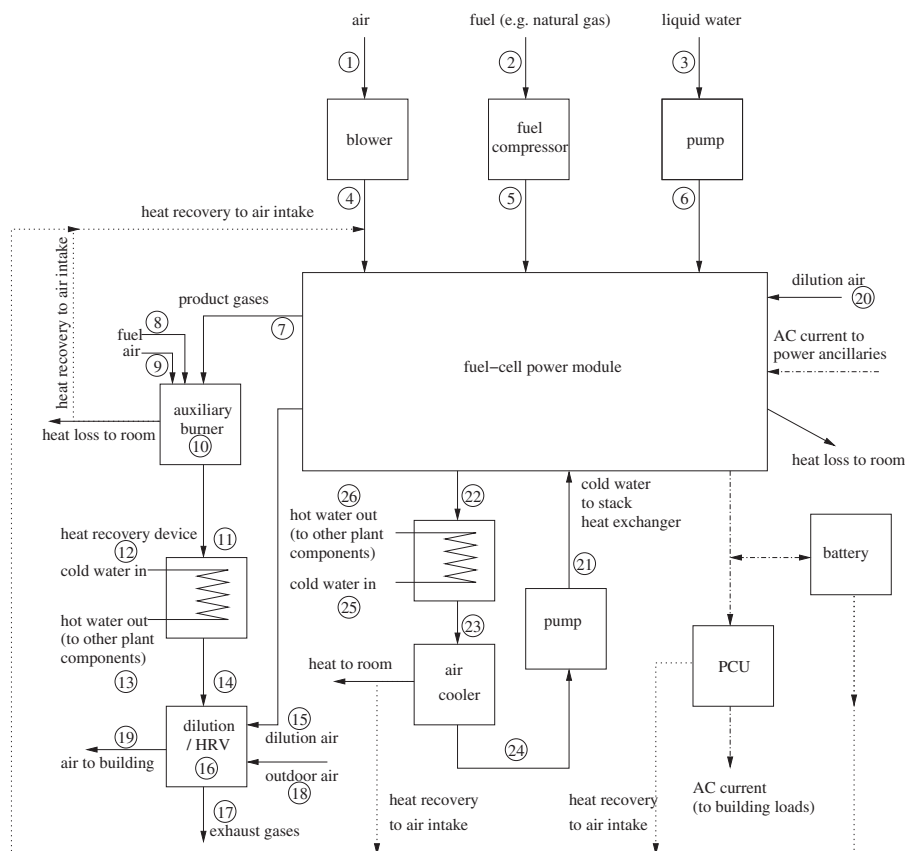

Fig. 1. Annex 42 fuel-cell micro-cogeneration model.

Although the Annex 42 model was developed to represent both SOFC and PEMFC devices, to date the model has not been calibrated to represent the performance of an actual PEMFC micro-cogeneration device. Furthermore, the appropriateness of the model's functional form for treating PEMFC systems has not been confirmed using measured data. The current paper makes a contribution to this field of study by examining the suitability of the Annex 42 model for representing PEMFC devices, proposing some improvements, and then calibrating the revised model to represent the performance of a 1.0 kW$_{AC}$ PEMFC micro-cogeneration device. Experimental data were gathered from 52 steady-state and 4 transient tests, which collectively constitute a performance map of the device. The design of the experiments and a description of the instrumentation employed are provided, and an analysis of the propagation of measurement uncertainties into derived quantities is presented. The procedures used to calibrate the Annex 42 model to represent the device are then detailed, following which a validation of the calibrated model is provided by contrasting model predictions to measurements taken from an additional 10 tests that were not included in the calibration data set. To begin, some pertinent aspects of the Annex 42 model are highlighted and improvements are proposed to provide the necessary context for the sections that follow.

2. Model description

As described in the introduction, the Annex 42 model can be configured to represent either a SOFC or a PEMFC micro-cogeneration device. A detailed description of aspects of the model critical to the treatment of SOFCs and their calibration was provided by Ref. [8]. This section supplements that material by focusing on the aspects of the model that are unique to the treatment of PEMFCs.

A number of the control volumes included in the Annex 42 model are not pertinent to PEMFC devices. States 7–19 shown on the left side of Fig. 1 refer to working fluid states relevant to the gas–water heat exchanger that is used to produce the useful thermal output in SOFC systems, as well as an optional auxiliary burner and a dilution air heat recovery ventilator (HRV). These components do not exist in PEMFC systems. Rather, a water–water heat exchanger that recovers thermal energy from the PEMFC stack produces the useful thermal output (see states 21–26 in the bottom–center of Fig. 1).

The Annex 42 model represents the stack cooling loop in detail. The stack coolant fluid is circulated by a pump (states 24–21) to the FCPM's internal heat exchanger where it recovers the heat that is generated by electrochemical processes (states 21–22). The stack coolant fluid then passes through a water–water heat exchanger (called the external heat exchanger, states 22–23), where energy is transferred to an external coolant stream (states 25–26). This external coolant stream is connected to the plant network that exploits this thermal output to supply the building's space and/or water heating needs. The Annex 42 model also includes an air cooler (states 23–24) in the stack cooling loop that is present in some PEMFC micro-cogeneration devices for rejecting additional heat to regulate the stack temperature. Methods are prescribed in the Annex 42 model for resolving the pump, the FCPM's internal heat exchanger, the external water–water heat exchanger, and the air cooler [7].

This explicit representation of the stack cooling loop was added to the Annex 42 model to support the representation of PEMFC devices. However, as the model was never calibrated to represent the performance of an actual PEMFC micro-cogeneration device, the practicality of this approach was never assessed. Some disadvantages of these aspects of the Annex 42 model have become

apparent during the current study. Firstly, it would be excessively difficult to implement in practice the instrumentation required to measure the thermal and electrical performance of the pump and air cooler. Furthermore, the calibration of the external water–water heat exchanger requires measuring the flow rate and temperature of the stack coolant fluid at states 22 and 23, necessitating invasive measurements. Finally, the method recommended for modeling the external water–water heat exchanger is not well supported in the literature and is cast in a functional form that is not pragmatic to calibrate.

For the reasons cited above, an alternate method is proposed here for treating the stack cooling loop. Rather than attempting to resolve the sub-components of the stack cooling loop (pump, air cooler, internal heat exchanger), with this method the stack cooling is treated in a manner that is pragmatic from a model calibration perspective. It recognizes that it is only practical to directly measure the flow rate and temperatures in the external-cooling-stream side of the external water–water heat exchanger, that is states 25 and 26. This alternate method preserves the structure of the Annex 42 model, but essentially nullifies the air cooler, pump, and internal heat exchanger in the stack cooling loop, and makes no attempt to solve state points 21 through 24. Rather, an energy balance is formed on the external heat exchanger that equates the thermal energy released by the FCPM to the thermal energy increase in the external-cooling-stream side of the external water–water heat exchanger. If it is assumed that the heat loss from the external heat exchanger is negligible and that the heat capacity of the fluid stream remains constant through the heat exchanger, then the energy balance can be written as,

$$q_{s\text{-cool}} = \left(\dot{N} \widehat{c}_P \right)_{\text{w}} \cdot (T_{\text{w-out}} - T_{\text{w-in}}) \tag{1}$$

where $q_{s\text{-cool}}$ is the heat released by the FCPM (W). $\dot{N}$ is flow rate of the external coolant through the heat exchanger (kmol s^{-1}) and $\widehat{c}_P$ is its heat capacity (J kmol^{-1} $^\circ$C^{-1}). $T_{\text{w-in}}$ is the temperature of the coolant stream entering the heat exchanger (state 25 in Fig. 1) and $T_{\text{w-out}}$ is the temperature of water exiting the heat exchanger (state 26).

In the Annex 42 model $q_{s\text{-cool}}$ is determined as a third-order parametric function of the FCPM's net DC power production (P_{el}, in W). The measurements gathered in the present study revealed that $T_{\text{w-in}}$ was also a significant determinant of $q_{s\text{-cool}}$. Consequently, an alternate functional form is proposed,

$$q_{s\text{-cool}} = r_0 + r_1 \cdot P_{\text{el}}^{\alpha_0} + r_2 \cdot (T_{\text{w-in}} - T_0)^{\alpha_1} \tag{2}$$

where r_i, α_i, and T_0 are parameters to be determined by calibrating the dependent observations of $q_{s\text{-cool}}$ to the independently controlled boundary conditions P_{el} and $T_{\text{w-in}}$. In the model's implementation, Equation (2) is used to determine $q_{s\text{-cool}}$ and this value is subsequently employed in Equation (1) to determine $T_{\text{w-out}}$.

The derivation of the r_i, α_i, and T_0 parameters and those for characterizing other aspects of the PEMFC micro-cogeneration device will be described in Section 5. The next section describes the experimental methods employed to gather the data necessary to perform these calibrations.

3. Experimental methods

3.1. Experimental configuration

A schematic representation of the experimental configuration is illustrated in Fig. 2. The fuel-cell was configured to draw air from the surrounding laboratory environment and was supplied with
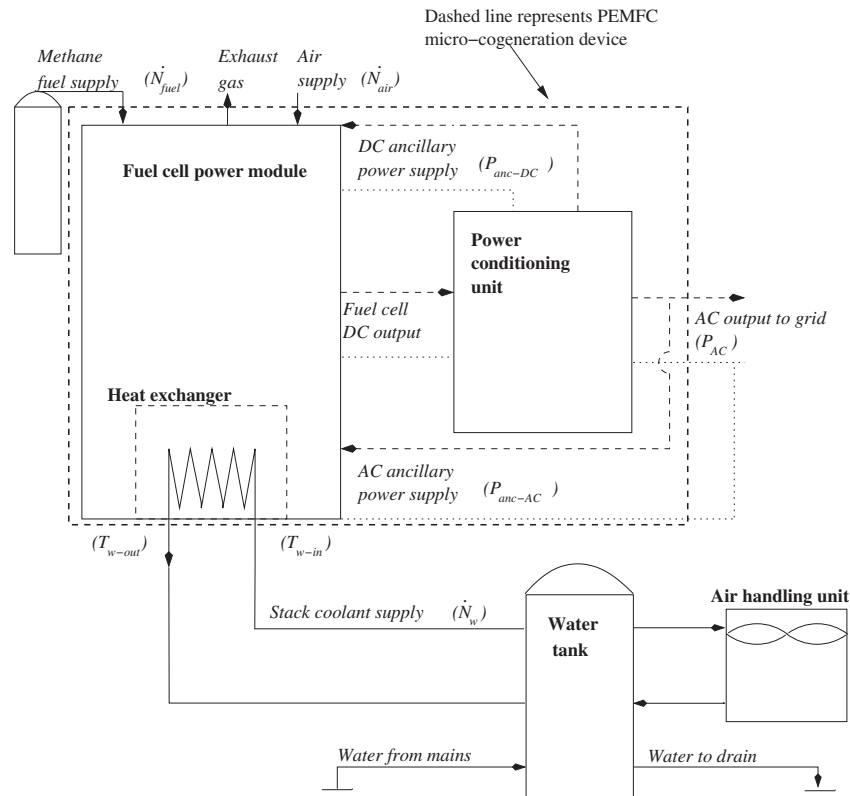
Fig. 2. Schematic representation of the experimental configuration.

methane from cylinders. Coolant water was supplied to the PEMFC's heat exchanger from a tank. The temperature of the tank could be controlled by rejecting energy from the tank through a water–air heat exchanger in an air-handling unit. The tank's temperature could also be controlled by drawing off hot water and replacing it with cold water from the city mains. An experimental plan was designed according to Ref. [17] to characterize the performance of the PEMFC micro-cogeneration device under precisely controlled operating conditions using this setup.

Two variables were controlled in the experiments. The first was the temperature of the coolant water supplied to the PEMFC, $T_{\text{w-in}}$ (refer to Fig. 2). The second was a control setting on the device that determined the AC power supplied to the grid, P_{AC}. The target range over which these variables were controlled and the nominal values achieved in the experiments are given in Table 1.

The PEMFC micro-cogeneration device's control system would respond to these boundary conditions by modulating a number of variables pertinent to the model's calibration, for example the fuel ($\dot{N}_{\text{fuel}}$) and air ($\dot{N}_{\text{air}}$) supply rates. As well, it would modulate the temperature of the exiting coolant water ($T_{\text{w-out}}$) by controlling an internal pump that determined the coolant water flow rate ($\dot{N}_{\text{w}}$) through the device. Consequently, the DC and AC ancillary power consumption ($P_{\text{anc-DC}}$ and $P_{\text{anc-AC}}$) were determined by the PEMFC micro-cogeneration device's control system's response to the externally controlled boundary conditions.

Steady-state tests were conducted for each of the combinations of $T_{\text{w-in}}$ and P_{AC} given in Table 1. Each test lasted about 60 min. After a stabilization period, during which the boundary conditions were monitored to ensure that steady-state conditions had been achieved, the data were logged for a period of about 30 min. The duration of these periods was chosen to allow for enough data to be logged such that the precision index (see Section 4) would be negligible for most cases. These data were utilized to derive the steady-state performance parameters that were used to calibrate the model, as detailed in later sections of the paper.

3.2. Instrumentation and measurement methods

Thorsteinson et al. [18] describe the development of the experimental apparatus that was used to operate the PEMFC micro-cogeneration device and to control the external boundary conditions discussed above. A number of important modifications were made to the experimental apparatus described in this earlier work in order to reduce experimental uncertainty. Firstly, to reduce the uncertainty in predicting the heating value of the fuel supply, the device was operated with tanks of methane rather than utility-supplied natural gas. The composition of the fuel supply and its impact on experimental uncertainty are described in Section 4.3.

Secondly, some of the instrumentation was modified to accord with Fig. 3. The types of measurements taken and the sensors employed are listed in Table 2. The gross DC power output (P_{DC}) was derived from current (I_{DC}) and voltage (V_{DC}) measurements, taken with a current shunt and voltage divider respectively. The same methods were used to determine the DC ancillary power supply ($P_{\text{anc-DC}}$) from current ($I_{\text{anc-DC}}$) and voltage ($V_{\text{anc-DC}}$) measurements. The net AC power output to the grid (P_{AC}) was measured directly by a meter that combined a current transformer and a voltmeter. The AC current output to the grid (I_{AC}) was separately measured with

Table 1
Operating range and experimentally achieved values for externally controlled boundary conditions.

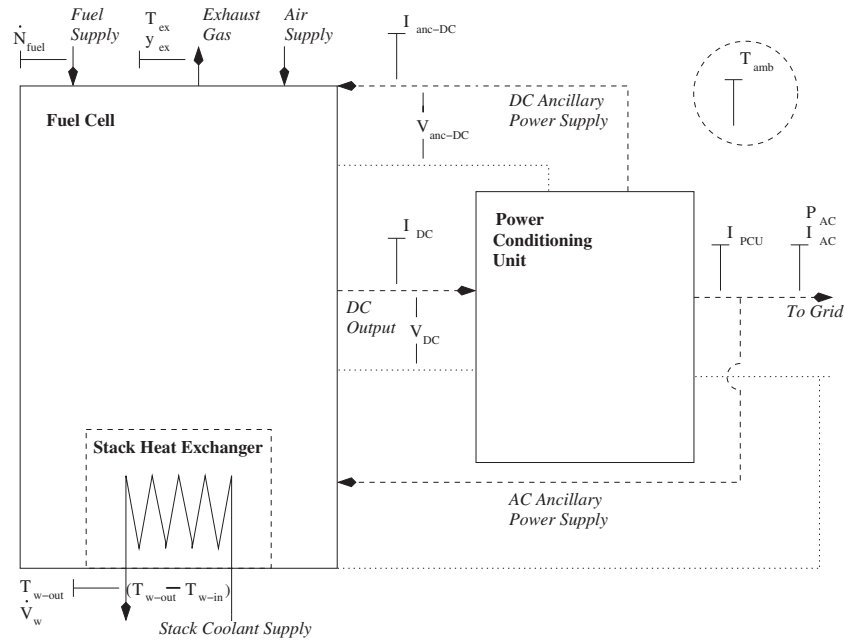| boundary condition	Operating range	Experimentally investigated values
$T_{\text{w-in}}$	15–60 °C	16, 20, 25, 30, 35, 40, 45, 55, 59 °C
P_{AC}	250–1000 W	272, 540, 750, 980 W

Fig. 3. Instrumentation placement.

a second current transformer. The AC ancillary current (I_{anc-AC}) and the AC current output by the PCU (I_{PCU}) were also measured with current transformers.

The temperature rise of the coolant through the heat exchanger ($\Delta T_w = T_{w-out} - T_{w-in}$ in °C) was measured directly with a pair of matched RTDs with calibrated wire lengths sensed by a revenue grade heat meter. T_{w-out} was measured with one RTD of the matched pair that was located at the heat exchanger's outlet. T_{w-in} was derived from measurements of ΔT and T_{w-out}. The flow rate of the coolant through the heat exchanger ($\dot{N}_w$ in kmol s^{-1}) was derived from measurements of the volumetric flow rate ($\dot{V}_w$ in L min^{-1}) taken with an ultrasonic flow meter and determination of the coolant's density from its temperature at the heat exchanger inlet (T_{w-in} in °C).

The rate of fuel supplied to the PEMFC micro-cogeneration device ($\dot{N}_{fuel}$ in kmol s^{-1}) was measured directly with a Coriolis mass flow meter. The ambient temperature of the laboratory housing the experiment was also sensed (T_{amb} in °C) as were the exhaust gas temperature (T_{ex} in °C) and dry molar percentage of CO_2 in the exhaust gas (y_{ex}).

Most of the instruments were sensed and their data logged by a data acquisition system (DAQ) at an interval of 6 s. There were several exceptions to this. T_{w-out} and ΔT_w were logged by a heat meter that subsequently output these data to the DAQ. However,

Table 2
Sensor types and measured parameters.

Primary measurement	Sensed quantity	Sensor type
T_{w-out}, T_{amb}, T_{ex}	Temperature	Resistance temperature detector (RTD)
ΔT_w	Temperature difference	Matched RTDs
$\dot{V}_w$	Volumetric flow rate	Ultrasonic flow meter
$\dot{N}_{fuel}$	Molar flow rate	Coriolis flow meter
y_{ex}	Dry molar percentage of CO_2	Non-dispersive infrared absorption
P_{AC}	AC power	Current transformer and voltmeter
I_{PCU}, I_{anc-AC}	AC current	Current transformer
V_{DC}, V_{anc-DC}	DC voltage	Voltage divider
I_{DC}, I_{anc-DC}	DC current	Current shunt

the heat meter produced its output at a lower frequency, sending a signal to the DAQ every 72 s. P_{AC} was directly logged by a separate computer. To ensure synchronization between these measurements and those taken with the DAQ, the clocks of the computer and the DAQ were synchronized daily.

The next section describes how these primary measurements were used to derive the thermal and electrical performance parameters necessary to calibrate the model.

4. Analysis of measurements and treatment of uncertainty

4.1. Instrumentation bias errors

The method recommended by the American Society of Mechanical Engineers [19,20] was used to propagate the individual sources of bias errors associated with each primary measurement,

$$B_P = \left[B_1^2 + B_2^2 + \ldots + B_j^2 \right]^{1/2} \tag{3}$$

where B_P is the overall bias error associated with a primary measurement. B_1, B_j, etc. are individual sources of bias errors for that measurement, such as imperfections in calibration curves, the bias of a resistor in a current shunt, the resolution of the DAQ for reading voltage signals, etc. This method assumes that each source of bias is independent.

All possible individual sources of bias errors were accounted for and Equation (3) was applied to determine the value of B_P for each of the primary measurements. These values are given in Table 3. A series of verification tests were then performed during which the measurements taken with a number of the instruments listed in Table 2 were compared to values determined with reference instruments. For example, the matched RTD's were each submerged simultaneously in different constant temperature baths and their measurement of temperature difference was compared to reference RTDs that were also submerged. These verification tests spanned the range of values anticipated in the controlled experiments and in all cases confirmed that the B_P values determined with Equation (3) were reasonable.

Table 3
Bias errors and uncertainty for primary measurement quantities.

Measured quantity	B_P	$\overline{U}_{P.95}$
V_{DC}	0.5% of value	0.5% of value
I_{DC}	0.5% of value	0.5% of value
V_{anc-DC}	0.5% of value	0.5% of value
I_{anc-DC}	0.5% of value	0.5−0.7% of value
I_{PCU}	1.1% of value	1.1% of value
I_{AC}	1.1% of value	1.1% of value
P_{AC}	3.5−5.9% of value	3.5−5.9% of value
$\dot{N}_{fuel}$	0.7% of value	0.7% of value
$\dot{V}_w$	2.2−4.9% of value	2.2−6.5% of value
T_{w-out}	0.6 °C	0.6−0.8 °C
ΔT_w	0.8−1.5% of value (0.13−0.38 °C)	0.8−4.9% of value
y_{ex}	2.9−7.4% of value	2.9−7.4% of value

4.2. Uncertainty in primary measurements

As previously mentioned, tests were conducted under steady conditions and data were logged for a period of time (typically 30 min) to derive the calibration data. For each test, the average value of each primary measurement was determined over the test's duration. The precision index of the average value of each primary measurement was then determined as follows,

$$\overline{S}_P = \frac{1}{\sqrt{N}} \cdot \left[\frac{\sum_{i=1}^{N} (X_i - \overline{X})^2}{N-1} \right]^{1/2} \tag{4}$$

where S_P is the precision index of the average value, N is the number of instantaneous measurements logged over the steady period, X_i is the instantaneous value of the primary measurement, and $\overline{X}$ is the corresponding average value.

The overall bias errors determined with Equation (3) and the precision indices determined with Equation (4) were then combined to determine the uncertainty of the average of each primary measurement quantity at a 95% confidence interval,

$$\overline{U}_{P,95\%} = \sqrt{B^2 + \left(t \cdot \overline{S}_P \right)^2} \tag{5}$$

where $\overline{U}_{P,95\%}$ is the uncertainty of the averaged value. t is the statistical Student's t-value and depends on the number of instantaneous measurements used to determine the average.

The $\overline{U}_{P,95\%}$ values associated with each primary measurement quantity over the range of values measured during the steady-state tests are provided in Table 3. In most cases the higher levels of uncertainty are associated with measurements of smaller quantities, particularly in the case of electrical currents, flow rates, and temperature differences. By contrasting the B_P and $\overline{U}_{P,95\%}$ values in this table, it can be seen that in most cases the bias errors are the dominant contributor to uncertainty. The exception to this is with ΔT_w, where it was found that the precision index dominated in some cases because of the lower sampling frequency of the heat meter (refer to Section 3.2).

4.3. Uncertainty in fuel's heating value

As previously stated, the experiments were conducted with tanks of methane rather than utility-supplied natural gas to reduce the uncertainty in predicting the fuel's heating value. The composition was certified to be 99% methane. A bias error on the fuel's lower heating value (LHV) was assigned based upon the unknown concentration of the remaining 1%. In the extreme, if the remaining gas was inert or entirely ethane, this would affect the LHV by 1%. Consequently, a bias error of 1% was assigned to the fuel's LHV.

4.4. Propagation of uncertainty into derived quantities

Similar methods were used to propagate primary measurement bias errors and precision errors into the derived quantities that are required to calibrate the model. This can be shown by an example focusing upon the derivation of the FCPM's DC power output from primary measurements of current and voltage,

$$P_{DC} = V_{DC} \cdot I_{DC} \tag{6}$$

The biases associated with the primary measurements can be propagated according to,

$$B_{P_{DC}} = \left[\left(\frac{\partial P_{DC}}{\partial V_{DC}} \cdot B_{V_{DC}} \right)^2 + \left(\frac{\partial P_{DC}}{\partial I_{DC}} \cdot B_{I_{DC}} \right)^2 \right]^{1/2} \tag{7}$$

where $B_{P_{DC}}$ is the bias error of the derived power and $B_{V_{DC}}$ and $B_{I_{DC}}$ are the bias errors for the primary measurements determined with Equation (3).

The precision index of the derived power is determined by evaluating Equation (6) at each of the instantaneous measurement intervals and then evaluating Equation (4) using the results. Likewise, the uncertainty of the derived quantity is then determined using Equation (5).

The techniques elaborated above were applied to calculate each derived quantity and its associated uncertainty. The next section describes how these data were then used to calibrate the model.

5. Model calibration

The methods described in Section 3 were applied to conduct a series of 52 steady-state and 4 transients tests with the PEMFC micro-cogeneration device. Of the 52 steady-state tests that were performed, the data required to calibrate the PCU efficiency and AC ancillary models of Sections 5.3 and 5.4 were only available for 46 tests. Of the 52 steady-state tests that were performed, the data required to calibrate the air flow and skin loss models of Sections 5.5 and 5.6 were only available for 40 tests.

The primary measurements were analyzed with the techniques detailed in Section 4 to produce the data required to calibrate the model described in Section 2. The calibration methods employed and the resulting model calibration parameters are presented here. Each of the following subsections focuses upon an individual aspect of the model.

5.1. FCPM electrical efficiency

In the Annex 42 model the FCPM's electrical efficiency (ε_{el}) is expressed as the net DC power production relative to the fuel's LHV,

$$\varepsilon_{el} = \frac{P_{el}}{\dot{N}_{fuel} \cdot LHV_{fuel}} \tag{8}$$

Since the model groups the fuel-cell stack with other components such as the fuel processor into the FCPM control volume, it makes no attempt to simulate the electrochemical processes occurring within the fuel cell, but rather represents the performance of the FCPM using a parametric relation between the electrical efficiency and the net electrical power output,

$$\varepsilon_{el} = \varepsilon_0 + \varepsilon_1 \cdot P_{el} + \varepsilon_2 \cdot P_{el}^2 \tag{9}$$

where ε_i are empirical coefficients that are to be established through calibration to measured data.

At each of the measurement points from each of the 52 steady-state experiments, the primary measurements were used to evaluate the instantaneous electrical efficiency,

$$\varepsilon_{el} = \frac{V_{DC} \cdot I_{DC} - V_{anc\text{-}DC} \cdot I_{anc\text{-}DC}}{\dot{N}_{fuel} \cdot LHV_{fuel}} \tag{10}$$

The derived ε_{el} values from one of the steady-state test are shown in Fig. 4. The average value of ε_{el} over the duration of this test is shown on the right side of the figure. The uncertainty of each instantaneous measurement point as well as the uncertainty in the test-averaged ε_{el} are shown. This figure illustrates how well steady conditions were maintained during the test, and how the bias errors dominated the uncertainty.

The test-averaged ε_{el} was determined for each of the 52 steady-state tests. These are shown in Fig. 5 as a function of the test-averaged P_{el}. This figure illustrates that ε_{el} is primarily determined by P_{el}, and thus confirms the appropriateness of the functional form of the Annex 42 model's Equation (9).

A least-squares regression was performed on Equation (9) to establish the values of the ε_i coefficients that produced the best fit to the data plotted in Fig. 5. The values of the coefficients determined from this analysis are presented in Table 4.

Fig. 5 also compares the ε_{el} determined with Equation (9) and the coefficients of Table 4 with the ε_{el} values derived from the measurements. The $\overline{U}_{95\%}$ uncertainty bars are plotted in the figure. The calibrated values lie within the $\overline{U}_{95\%}$ uncertainty bars for 36 of the 52 tests. Another indication of the goodness of fit is provided by Fig. 6. The coefficient of determination (r^2 value) was 0.92. The average error (difference between the calibrated ε_{el} value and that derived from measurements) was 1.1% (in relative terms) while the root-mean-square error was 1.5%. The maximum error for a single point was 4.6%.
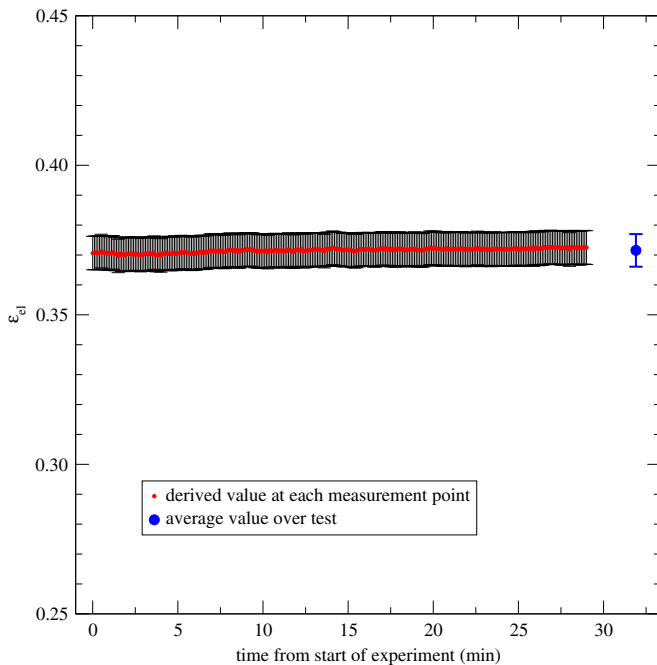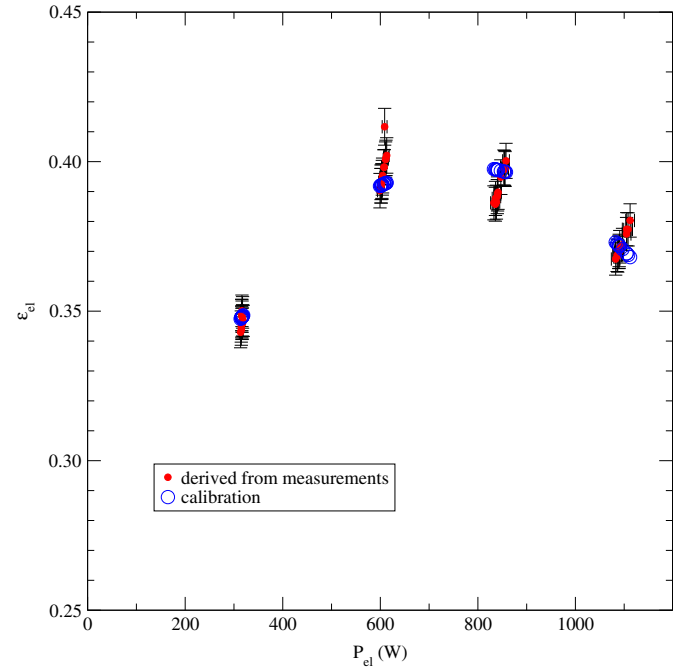

Fig. 5. Test-averaged FCPM electrical efficiencies for each of the 52 steady state tests.

5.2. Heat recovery

Similar methods were used to calibrate Equation (2), but in this case a non-linear regression method was employed. The r_i, α_i, and T_0 parameters that produced the best fit to the values of $q_{s\text{-}cool}$ derived from the primary measurements using Equation (1) are given in Table 4.

Fig. 7 compares the $q_{s\text{-}cool}$ determined with Equation (2) and the parameters of Table 4 with the $q_{s\text{-}cool}$ values derived from the measurements. The left side of the figure examines the variation with $T_{w\text{-}in}$ whereas the right side considers P_{el}. As can be seen, the functional form of Equation (2) well represents the dependency of $q_{s\text{-}cool}$ on the experiment's two independent variables. The calibrated values lie within the error bars for 38 of the 52 steady-state tests.

Fig. 8 provides another indication of the goodness of fit between the calibrated $q_{s\text{-}cool}$ values and those derived from measurements over the full operating range. The coefficient of determination (r^2 value) was 0.997. The average error (difference between the calibrated $q_{s\text{-}cool}$ value and that derived from measurements) was

Table 4
Calibration coefficients.

FCPM electrical efficiency coefficients for Equation (9)	$\varepsilon_0 = 2.5111 \times 10^{-1}$; $\varepsilon_1 = 3.8642 \times 10^{-4}$; $\varepsilon_2 = -2.529 \times 10^{-7}$
Heat recovery parameters for Equation (2)	$r_0 = 2.0417 \times 10^2$; $r_1 = 1.8522 \times 10^{-2}$; $r_2 = -1.664 \times 10^{-1}$; $\alpha_0 = 1.6$; $\alpha_1 = 2$; $T_0 = 26.5$
PCU efficiency coefficients for Equation (12)	$u_0 = 9.1332 \times 10^{-1}$; $u_1 = 6.7317 \times 10^{-5}$; $u_2 = -6.406 \times 10^{-8}$
AC ancillary power consumption coefficients for Equation (14)	$anc_0 = 1.6619 \times 10^1$; $anc_1 = 3.8580 \times 10^6$
Air flow coefficients for Equation (16)	$a_0 = -3.217 \times 10^{-6}$; $a_1 = 2.1421 \times 10^1$; $a_2 = -1.261 \times 10^6$
Skin loss parameters for Equation (17)	$s_0 = 2.1070 \times 10^2$; $s_1 = 1.0979 \times 10^{-4}$; $s_2 = 2.1256 \times 10^{-1}$; $\beta_0 = 2$; $\beta_1 = 2$; $T_1 = 28.2$
Range of applicability: 16.1 °C $\leq T_{w\text{-}in} \leq$ 59.1 °C 314 W $\leq P_{el} \leq$ 1113 W $T_{room} \approx 22$ °C	

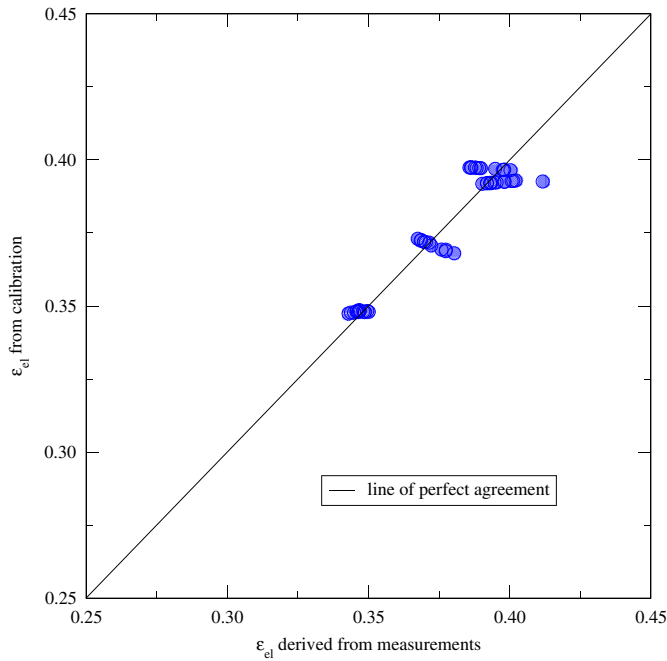Fig. 4. Derived values of FCPM electrical efficiency for one steady-state test.

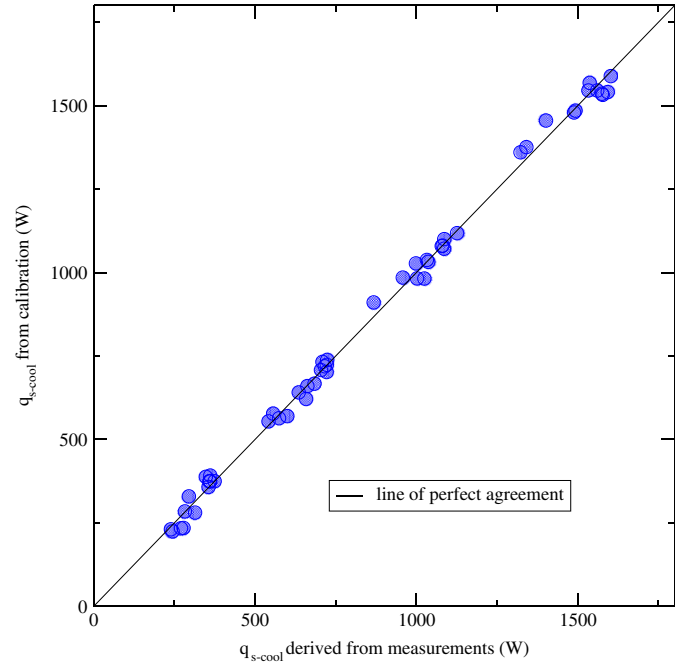**Fig. 6.** Goodness of fit between calibrated and measured ε_{el}.

Fig. 8. Goodness of fit between calibrated and measured $q_{s\text{-}cool}$.

3.3% while the root-mean-square error was 4.9%. The maximum error for a single point was 15.7%.

5.3. Power conditioning unit

In the Annex 42 model the PCU efficiency (η_{PCU}) is given by,

$$\eta_{PCU} = \frac{P_{PCU}}{P_{el}} \tag{11}$$

where P_{PCU} is total amount of AC power output from the PCU.

A polynomial expression is used to relate η_{PCU} to the PCU's DC input,

$$\eta_{PCU} = u_0 + u_1 \cdot P_{el} + u_2 \cdot P_{el}^2 \tag{12}$$

where u_i are empirical coefficients that are to be established through calibration to measured data.

The primary measurements were used to evaluate Equation (11) for each measurement point,

$$\eta_{PCU} = \frac{P_{AC} \cdot \frac{I_{PCU}}{I_{AC}}}{I_{DC} \cdot V_{DC} - I_{anc\text{-}DC} \cdot V_{anc\text{-}DC}} \tag{13}$$

The relevant data to derive η_{PCU} were only available for 46 steady-state tests. The test-averaged η_{PCU} was determined for each
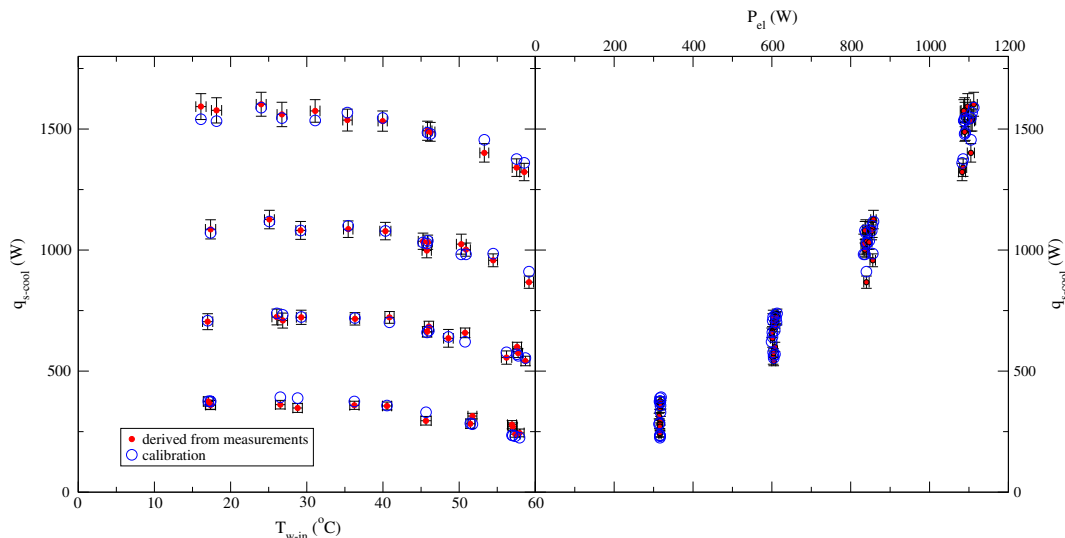

Fig. 7. Test-averaged heat recovery for each of the 52 steady-state tests.

of these 46 steady-state tests and a least-squares regression performed to determine the u_i coefficients that best fit these data to Equation (12). These coefficients are given in Table 4.

Figs. 9 and 10 contrast the η_{PCU} values derived from the measurements to those predicted with Equation (12) using the coefficients of Table 4. As can be seen, the calibrated values lie within the error bars for all 46 of the steady-state tests for which the relevant data were available. The coefficient of determination (r^2 value) was 0.89. The average error (difference between the calibrated η_{PCU} value and that derived from measurements) was 0.2% (in relative terms) while the root-mean-square error was 0.3%. The maximum error for a single point was 1.0%.

5.4. AC ancillaries

The Annex 42 model uses a polynomial expression to relate the AC ancillary power draws to the rate of fuel consumption,

$$P_{anc\text{-}AC} = anc_0 + anc_1 \cdot \dot{N}_{fuel} \tag{14}$$

where anc_i are empirical coefficients that are to be established through calibration to measured data.

The AC ancillary power draws were derived from the primary measurements for each measurement point according to,

$$P_{anc\text{-}AC} = \frac{I_{PCU} - I_{AC}}{I_{AC}} \cdot P_{AC} \tag{15}$$

The relevant data to derive $P_{anc\text{-}AC}$ were only available for 46 steady-state tests. The test-averaged $P_{anc\text{-}AC}$ were determined for each of these 46 steady-state tests and a least-squares regression performed to determine the anc_i coefficients that best fit these data to Equation (14). These coefficients are given in Table 4.

Figs. 11 and 12 contrast the $P_{anc\text{-}AC}$ values derived from the measurements to those predicted with Equation (14) using the coefficients of Table 4. As can be seen, the calibrated values lie within the error bars for all 46 of the steady-state tests for which the relevant data were available. The coefficient of determination (r^2 value) was 0.94. The average error (difference between the calibrated $P_{anc\text{-}AC}$ value and that derived from measurements) was
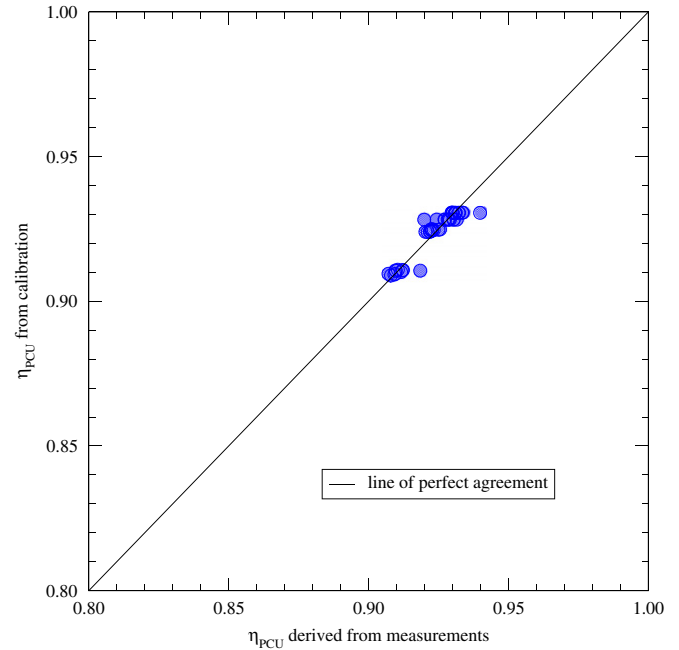

Fig. 10. Goodness of fit between calibrated and measured η_{PCU}.

2.8% while the root-mean-square error was 3.8%. The maximum error for a single point was 12%.

5.5. Air supply

The Annex 42 model provides three optional methods for treating air supply. The method that expresses the air supply as a function of the fuel's flow rate was chosen for this work,

$$\dot{N}_{air} = \left[a_0 + a_1 \cdot \dot{N}_{fuel} + a_2 \cdot \dot{N}_{fuel}^2 \right] \cdot [1 + a_3 \cdot T_{air}] \tag{16}$$
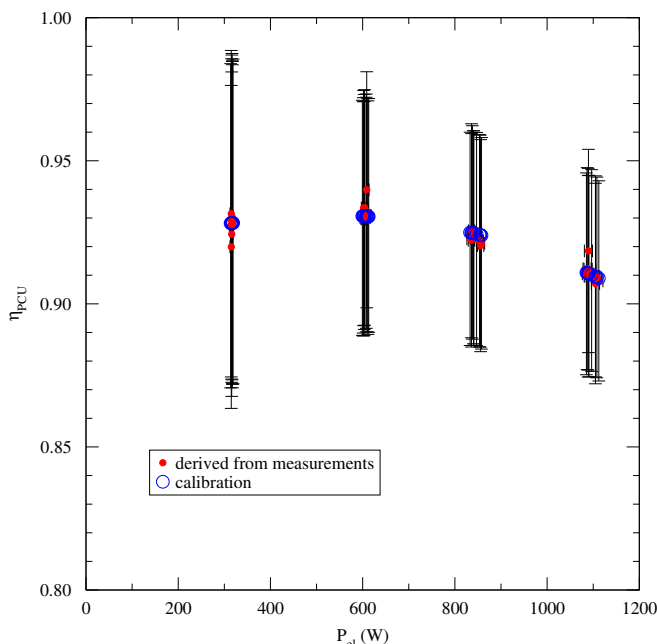

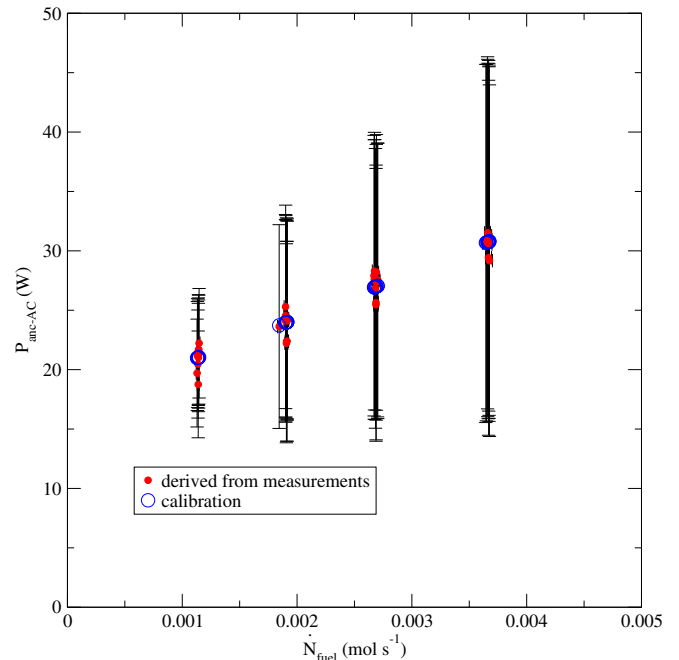**Fig. 9.** Test-averaged PCU efficiency for 46 of the steady-state tests.

Fig. 11. Test-averaged AC ancillary power consumption for 46 of the steady-state tests.
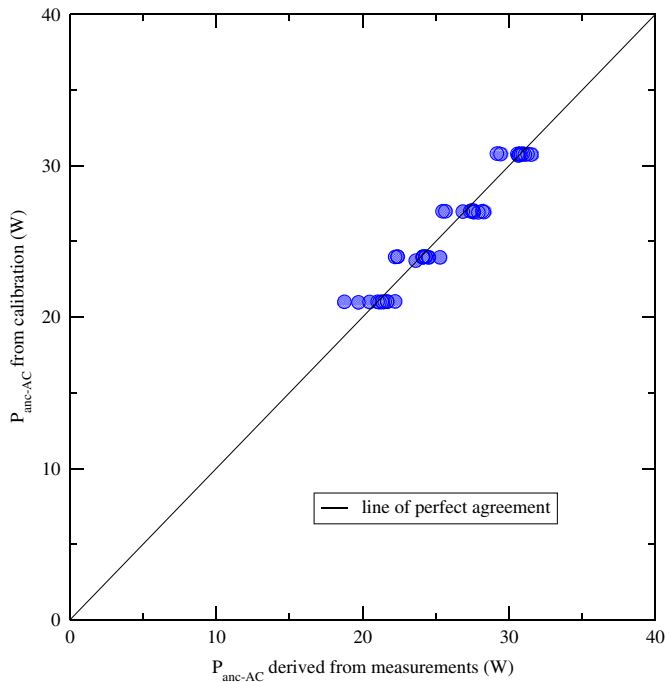
Fig. 12. Goodness of fit between calibrated and measured $P_{\text{anc-AC}}$.

where a_i are empirical coefficients that are to be established through calibration to measured data. T_{air} is the temperature of the supply air, which is assumed to be at T_{amb}, the temperature of the air in the surrounding laboratory environment from which the PEMFC micro-cogeneration device draws air.

Since all experiments were conducted with approximately the same value of T_{air}, no attempt was made to calibrate the coefficient a_3 in Equation (16), and as a consequence, the resulting calibration ignores any temperature dependence on air supply.

The primary measurements of $\dot{N}_{\text{fuel}}$ and the exhaust gas composition y_{ex} were used to determine how much excess oxygen was contained in the exhaust. When combined with a stoichiometric analysis, this yielded an estimation of $\dot{N}_{\text{air}}$. The values estimated for each steady-state test were then used to calibrate Equation (16) using a least-squares approach. The relevant data to derive $\dot{N}_{\text{air}}$ were only available for 40 of the steady-state tests.

The resulting a_i coefficients are given in Table 4. The calibrated values lie within the error bars for 20 of the 40 steady-state tests for which the relevant data were available. The coefficient of determination (r^2 value) was 0.99%. The average error (difference between the calibrated $\dot{N}_{\text{air}}$ value and that derived from measurements) was 3.5% while the root-mean-square error was 4.5%. The maximum error for a single point was 11.6%.

5.6. Skin losses

The Annex 42 model provides three optional methods for treating parasitic thermal losses, or skin losses, which is the unintended heat transfer from the device to the containing room. Although this aspect of the model does not influence the prediction of electrical output or useful thermal output, this heat loss can influence the thermal environment within the building.

Based upon an analysis of the data, it was determined that the three methods provided in the Annex 42 model were inadequate for characterizing this PEMFC micro-cogeneration device because they neglected the effect of $T_{\text{w-in}}$. Consequently, an alternate functional form is proposed here,

$$q_{\text{loss}} = s_0 + s_1 \cdot P_{\text{el}}^{\beta_0} + s_2 \cdot (T_{\text{w-in}} - T_1)^{\beta_1} \qquad (17)$$

where s_i, β_i, and T_1 are empirical parameters that are to be established through calibration to measured data.

The test-averaged value of q_{loss} was determined from the primary measurements through a heat balance method that considered the enthalpy flowing in with the fuel, P_{AC}, $q_{\text{s-cool}}$, and the flue losses. The relevant data to derive q_{loss} were only available for 40 of the steady-state tests. There was considerable uncertainty in deriving q_{loss} due to the difficulty in predicting the flue loss component of this heat balance. A non-linear curve fit procedure was then used to calibrate these data to Equation (17). The s_i, β_i, and T_1 parameters resulting from this process are provided in Table 4. The calibrated values lie within the error bars for 31 of the 40 steady-state tests for which the relevant data were available. The coefficient of determination (r^2 value) was 0.84. The average error (difference between the calibrated q_{loss} value and that derived from measurements) was 8% while the root-mean-square error was 10%. The maximum error for a single point was 29%. While these metrics indicate a poorer fit than was achieved with other aspects of the model, it must be recalled that the overall effect on accuracy should be minor; the maximum error in q_{loss} was approximately 85 W, which will have only a minor impact upon a room energy balance.

5.7. Transient response, startup, and shutdown

The Annex 42 model limits the transient response in three ways in an attempt to characterize the impact that physical dynamics and control behavior have on overall system performance. Firstly, the response during normal operation is characterized by maximum allowable time derivatives for P_{el}. These parameters limit how quickly the model can modulate in response to external control signals. A second set of inputs characterizes the startup period (duration, rates of fuel and electricity consumption, and rate of electricity production). A third set of inputs characterizes the shutdown period (duration and rates of fuel and electricity consumption).

Four transient tests were performed to estimate these values, which are provided in Table 5. The startup and shutdown parameters were observed to vary significantly in the various tests that were performed. Consequently, the uncertainty associated with those parameters should be considered high. Notwithstanding, this should have little significance upon model reliability since the PEMFC micro-cogeneration device under study was designed for near-continuous operation.

6. Validation

The previous section described how the various aspects of the model were calibrated. Following the methodology presented by Ref. [9], 10 steady-state tests were performed in addition to the

Table 5
Estimates of transient parameters.

| Symbol	Description	Estimate
$+\dfrac{dP_{\text{el}}}{dt}$	Net DC output power maximum rate of increase	0.61 W s^{-1}
$-\dfrac{dP_{\text{el}}}{dt}$	Net DC output power maximum rate of decrease	0.60 W s^{-1}
δt_{su}	Start-up duration	1.9 h
$E_{\text{el-su}}$	Net DC production during start-up	1.0 MJ
$E_{\text{anc-AC-su}}$	AC ancillary consumption during start-up	3.1 MJ
$N_{\text{fuel-su}}$	Fuel consumption during start-up	7.45×10^{-3} kmol
δt_{sd}	Shut-down duration	0.5 h
$E_{\text{anc-AC-sd}}$	AC ancillary consumption during shut-down	30 kJ
$N_{\text{fuel-sd}}$	Fuel consumption during shut-down	0.06×10^{-3} kmol
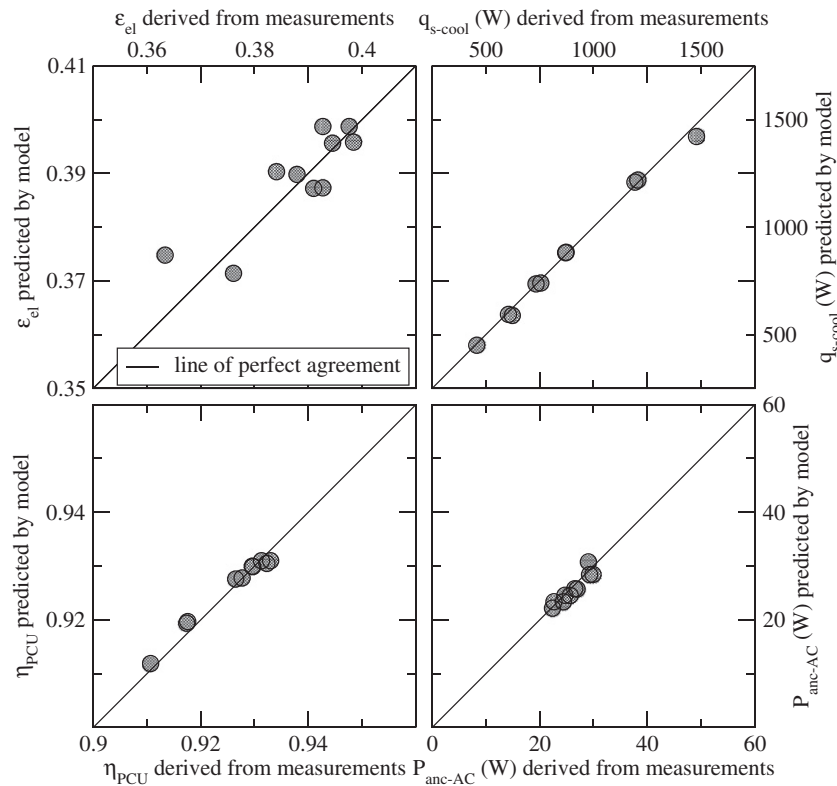
Fig. 13. Comparisons of four key model predictions for the 10 validation tests.

tests presented in the previous section to provide data for validating the model and its calibration. These 10 validation tests spanned boundary conditions within the same range as those employed in the calibration tests (see Table 1), but different combinations of P_{AC} and T_{w-in} were examined.

Test-averaged quantities were derived for these 10 validation tests using the methods previously elaborated. Then, calibrated model predictions were determined for ε_{el}, q_{s-cool}, η_{PCU}, and P_{anc-AC} using Equations (2), (8), (12) and (14) using the calibration coefficients from Table 4.

A comparison between the quantities derived from the measurements and those predicted with the calibrated model is presented in Fig. 13. An examination of each quadrant of the figure reveals that the calibrated model predictions are in good agreement with the measured data. Although the uncertainty bars are not shown in the figure for the sake of clarity, only 2 of the 10 points for q_{s-cool} and 3 of the 10 points for ε_{el} lie outside the 95% uncertainty range.

The average deviations between the calibrated model predictions and the values derived from measurements were found to be (in relative terms) 1.2% for ε_{el}, 2.0% for q_{s-cool}, 0.1% for η_{PCU}, and 3.4% for P_{anc-AC}. The greatest deviations were found to be 3.1% for ε_{el}, 5.4% for q_{s-cool}, 0.2% for η_{PCU}, and 5.9% for P_{anc-AC}. In all cases, the goodness of fit between the measurements and the model predictions was as good for the validation tests as for the calibration tests.

7. Conclusions

Previous research conducted by Annex 42 of the International Energy Agency's Energy Conservation in Buildings and Community Systems Programme produced a mathematical model for simulating the thermal and electrical performance of fuel-cell micro-

cogeneration devices which is suitable for use in whole-building simulation programs. This is a system-level model that considers the thermodynamic performance of all components that consume energy and produce thermal and electrical output. The model is discretized to represent 12 sub-systems, such as those that produce electrical power, convert DC to AC, and capture heat from hot product gases. Some of these control volumes are only pertinent to SOFC devices, whereas others apply uniquely to PEMFC devices. The Annex 42 model has previously been calibrated to represent the performance of a specific SOFC micro-cogeneration device, and the validity of the model's structure for representing such systems has been demonstrated. The current paper has extended this work by examining the ability of the Annex 42 model to represent PEMFC micro-cogeneration devices and by proposing some improvements to the model.

An experiment was configured and a series of tests were performed with a 1.0 kW$_{AC}$ PEMFC micro-cogeneration device. Instrumentation was selected, verified, and configured to minimize uncertainty and to gather all the data necessary to calibrate the model to represent this device. 52 tests were performed under steady boundary conditions and 4 under transient conditions to yield sufficient data to calibrate the model over the device's entire operating range.

An examination of these calibration data revealed some weaknesses in the Annex 42 model. Firstly, the treatment of the PEMFC stack cooling loop was found to be impractical for a model that must be calibrated using empirical data. Invasive measurements would be required to gather sufficient data to resolve some of the sub-systems. Given this shortcoming, an alternate approach has been proposed for modeling the stack cooling loop, one that was informed through an examination of the empirical data gathered on the tested device. The functional form of the Annex 42 model's

treatment of parasitic thermal losses was also found to be lacking. Again, a new formulation has been put forward based upon an examination of the measured data.

All pertinent sub-systems of the enhanced Annex 42 model were then calibrated using the data derived from the 52 steady-state and 4 transient calibration tests. The goodness-of-fit of the calibrations were discussed and all parameters required to execute the model to represent the 1.0 kW$_{AC}$ PEMFC micro-cogeneration device were presented. Finally, the validity of the functional form of the model and its calibration was tested by contrasting model predictions to measured data gathered from 10 additional tests that were disjunct from the calibration data set.

Future research will apply the calibrated model to examine the thermal and electrical performance of the 1.0 kW$_{AC}$ PEMFC micro-cogeneration device in various residential buildings, in various climates, and under various operating scenarios to contrast the performance of the technology to conventional heating and electrical supply systems. It also remains to be shown that the form of the PEMFC model developed in this paper is suitable to represent larger scale PEMFCs.

Acknowledgments

References

[1] IEA/ECBCS Annex 42 Reportl. Knight, V. Ugursal (Eds.), Residential Cogeneration Systems: A Review of the Current Technologies (2005), ISBN 0-662-40482-3.
[2] H. Onovwiona, V. Ugursal, Renewable and Sustainable Energy Reviews 10 (2006) 389–431.
[3] U.C. Colpier, D. Cornland, Energy Policy 30 (2002) 309–316.
[4] T. DeMoss, Power Engineering 100 (1996) 17–21.
[5] IEA/ECBCS Annex 42 Reportl. Beausoleil-Morrison (Ed.), An Experimental and Simulation-Based Investigation of the Performance of Small-Scale Fuel Cell and Combustion-Based Cogeneration Devices Serving Residential Buildings (2008), ISBN 978-0-662-47923-9.
[6] I. Beausoleil-Morrison, A. Schatz, F. Maréchal, HVAC&R Research Special Issue 12 (2006) 641–667.
[7] N. Kelly, I. Beausoleil-Morrison (Eds.), Specifications for Modelling Fuel Cell and Combustion-Based Residential Cogeneration Devices within Whole-Building Simulation Programs (2007), ISBN 978-0-662-47116-5. IEA/ECBCS Annex 42 Report.
[8] I. Beausoleil-Morrison, K. Lombardi, Journal of Power Sources 186 (2009) 67–79.
[9] I. Beausoleil-Morrison, Journal of Power Sources 195 (2010) 1416–1426.
[10] P. Kazempoor, V. Dorer, A. Weber, International Journal of Hydrogen Energy 36 (2011) 13241–13249.
[11] A. Contreras, F. Posso, E. Guervos, Applied Energy 87 (2010) 1376–1385.
[12] A. Arsalis, M. Nielsen, S. Koer, International Journal of Hydrogen Energy 36 (2011) 5010–5020.
[13] A. Arsalis, M. Nielsen, S. Koer, Energy 36 (2011) 993–1002.
[14] A. Arsalis, M. Nielsen, S. Koer, International Journal of Hydrogen Energy 37 (2012) 2470–2481.
[15] L. Martins, J. Gardolinski, J. Vargas, J. Ordonez, S. Amico, M. Forte, Applied Thermal Engineering 29 (2009) 3036–3048.
[16] F. Musio, F. Tacchi, L. Omati, P. Stampino, G. Dotelli, S. Limonta, P. Grassini, International Journal of Hydrogen Energy 36 (2011) 8045–8052.
[17] IEA/ECBCS Annex 42 Reportl. Beausoleil-Morrison (Ed.), Experimental Investigations of Residential Cogeneration Devices and Model Calibration (2007), ISBN 978-0-662-47523-1.
[18] E. Thorsteinson, B. Strathearn, G. Mackenzie, G. Amow, in: Proc. International Conference on Microgeneration and Related Technologies (2011). Glasgow, Scotland.
[19] R. Abernethy, R. Benedict, R. Dowdell, Journal of Fluids Engineering 107 (1985) 161–164.
[20] R. Moffat, Experimental Thermal and Fluid Science 1 (1988) 3–17.